High turnover frequency H_2 evolution electrocatalysis at low acid concentration promoted by bioinspired (NCS2)Ni(II) complexes

Soumalya Sinha,[†,#] Giang N. Tran,[†,#] Hanah Na,[†] Nigam P. Rath,[‡] and Liviu M. Mirica[†,]*

[†] Department of Chemistry, University of Illinois at Urbana-Champaign, 600 S. Mathews Avenue, Urbana, Illinois, 61801

[‡] Department of Chemistry and Biochemistry, University of Missouri-St. Louis, One University Boulevard, St. Louis, Missouri, 63121-4400

[#] These authors contributed equally.

*mirica@illinois.edu

KEYWORDS: electrocatalysis, hydrogen evolution reaction (HER), Ni(I) complexes, organometallic Ni complex.

ABSTRACT

Electrochemical proton reduction to produce hydrogen is considered a sustainable approach to shift the fossil fuel-based energy production toward renewable energy sources. Although the development of molecular electrocatalysts for the hydrogen evolution reaction (HER) has gained significant attention, most of these molecular catalysts require either strong acids or often operate

at high proton concentration to achieve high turnover. Herein, we report the synthesis and charcterization of two Ni^{II} complexes, $[(N2S2)Ni(MeCN)_2](OTf)_2$ (**1•(OTf)$_2$**) and $(NCHS2)Ni(OTf)_2$ (**2**) bearing bioinspired 3,7-dithia-1,5(2,6)-dipyridinacyclooctaphane (N2S2) and 3,7-dithia-1(2,6)-pyridina-5(1,3)-benzenacyclooctaphane (NCHS2) ligands, respectively, along with their electrochemical HER in a non-aqueous electrolyte. Our Ni complexes show high turnover frequencies greater than 200,000 s^{-1} in the presence of ≤0.043 M of trifluoroacetic acid with ≥1 M of water present. Under these electrochemical conditions, **2** exhibited 2.5-fold faster kinetics at 240 mV lower overpotential than that of $\mathbf{1}^{2+}$. Furthermore, **2** initiates electrochemical proton reduction at the potential where $Ni^{II/I}$ redox couple occurs, whereas the similar HER electrocatalysis carried out by $\mathbf{1}^{2+}$ was observed at the potential for the $Ni^{I/0}$ redox couple. The electrochemical analysis revealed that **2** undergoes an uncommon HER mechanism proposed to involve a Ni^{III}–hydride species – a typical pathway followed by [NiFe] hydrogenase enzymes, upon activating the C–H bond of the coordinating NCHS2 ligand, and the resulting organometallic Ni complex is proposed to be the active HER electrocatalyst. This organometallic Ni complex derivative, $[(NCS2)Ni(MeCN)_2]^{2+}$ (**5**) was synthesized independently and its performance for the HER supports the proposed HER mechanism for **2**. Additionally, electron paramagnetic resonance (EPR) spectroscopy was employed to probe the accessibility to Ni^{I} and Ni^{III} species proposed as intermediates in the described HER mechanisms. Importantly, comparative catalytic Tafel plots were constructed to benchmark the HER activity of $\mathbf{1}^{2+}$ and **2** versus previously reported known Ni-based HER electrocatalysts. Overall, the organometallic (NCS2)Ni system reported below represents a novel bioinspired molecular HER electrocatalyst that exhibits a high turnover frequency and more closely resembles the Ni^{I}/Ni^{III} HER mechanism proposed to pe operative in [NiFe] hydrogenases.

INTRODUCTION

Seeking sustainable and renewable energy resources to reduce the use of fossil fuels has become of the utmost importance where the central theme is to store solar energy into chemical energy.[1,2] Although construction of new energy infrastructure with low emission of carbon footprints is essential to mitigate the atmospheric greenhouse gas concentration, the required technologies that could overcome such challenges still need substantial fundamental development to match the similar benchmark as obtained by using fossil fuels. For example, fuel cells could be promising energy solutions in which H_2 is a key ingredient, but the production of H_2 as feedstock using precious metal like platinum impedes the commercialization of such technologies. Considering the potential use of H_2 as a "clean energy" carrier to supply electricity on demand, the production of H_2 using cheap and earth-abundant materials have gained impressive attention in recent times.[2-5] However, the objective is to achieve high turnover H_2 production at low overpotential by employing efficient electrocatalysts at mild reaction conditions.

In nature, biological catalysts such as [NiFe] hydrogenases perform proton reduction to H_2 reversibly with the turnover frequencies (TOFs) of ~1000 s^{-1} in weakly acidic aqueous solution at very low overpotential.[6-9] The [NiFe] hydrogenases comprise hetero-bimetallic complexes at their active site where two metal centers, Ni^{II} and Fe^{II} are bridged through two cysteine (Cys)-thiolate ligands and the Ni center is further coordinated with two terminal Cys, which play a role in the H^+ transfer events during H_2 oxidation- (HOR) or H_2 evolution reaction (HER).[10] However, the investigation of mechanistic aspects of such [NiFe] hydrogenases for HOR revealed three distinct states of their active site, Ni-SI_a, Ni-C, and Ni-R (Scheme 1).[11-13] Considering that [NiFe] hydrogenases can carry out both HOR and HER processes reversibly, an overall mechanism for the HER process was proposed[14] in which the Ni-SI_a state is the active intermediate that has two

open coordination sites for substrate binding (i. e., H^+ for HER) and undergoes a one electron reduction to yield a paramagnetic Ni-C state. This Ni-C state contains a hydride bridging ligand between Ni^{III} and Fe^{II} with a shorter Ni–H bond distance ($d_{Ni–H}$) than that of Fe–H ($d_{Fe–H}$). [10,15,16] Such reduction from the Ni-SI_a state to the Ni-C state could also involve an alternate intermediate Ni-L in which the Ni center is in the +1 oxidation state and one of the terminal Cys resides ligated to Ni is protonated.[17-19] Further $1H^+/1e^-$ reduction of the Ni-C state leads to the Ni-R state that releases H_2 and regenerates the Ni-SI_a state to complete the catalytic cycle. These Ni-L and Ni-C states of [NiFe] hydrogenases have been the inspiration for designing biomimetic catalysts for HER or HOR,[16,20-25] however research efforts to utilize those catalysts in practical devices have had limited success. Furthermore, there are very few reports on the synthesis of complexes proposed to contain a Ni^{III}-H species, [16,26-28] and no isolated and structurally characterized Ni^{III}-H complex has been reported to date.

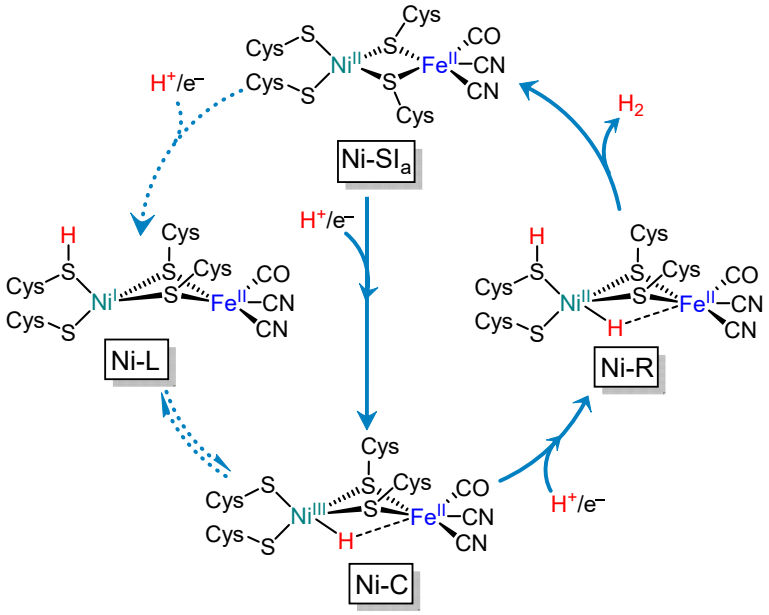

Scheme 1. Overall catalytic cycle for [NiFe] hydrogenases, shown in the direction of the HER process. The formation of the alternate Ni-L intermediate is shown with dotted arrows.

Although recently molecular electrocatalysts bearing first-row transition metals such as nickel,[29-32] cobalt,[33-35] or iron[36-38] have gained significant recognition in the library of different catalysts for HER, the formation of H_2 from $2H^+$ and $2e^-$ with high turnover under mild conditions is still challenging despite its thermodynamic simplicity. Accounting for the efficient and high turnover H_2 production strategies performed by hydrogenase enzymes in biological systems,[39,40] many synthetic models carrying a proton relay group in the second-coordination sphere have been investigated in the literature.[32,41-45] A great example among those is a Ni^{II} complex stabilized by 1,3,6-triphenyl-1-aza-3,6-diphosphacycloheptane, $[Ni(P^{Ph}{}_2N^{Ph})_2](BF_4)_2$, which shows HER with high turnover frequency (TOF) $\geq 10^5$ s^{-1}, in presence of dimethylformamide, $[(DMF)H]^+$ ($pK_{a[(DMF)H]}$ = 6.1 in MeCN)[46] as the proton source in the MeCN with 1.2 M of water.[32] More recently, Dempsey and co-workers have employed modified $P^{Ph}{}_2N^{Ph}$ ligand with an additional amine functionality and the corresponding Ni^{II} complex $[Ni(P^{Ph}{}_2N^{Ph}{}_2)_2](BF_4)_2$ ($P^{Ph}{}_2N^{Ph}{}_2$ = 1,3,5,7-tetraphenyl-1,5-diaza-3,7-diphosphacyclooctane) produces H_2 with higher TOF's in the presence of a weaker acid, anilinium ($pK_{a,\ anilinium}$ = 10.62 in MeCN)[46] in MeCN, but at higher acid concentrations (≥0.6 M).[47] Overall, the above examples of Ni^{II} based molecular HER electrocatalysts perform well for H_2 production in MeCN, either in the presence of stronger acids or at high acid concentration.

More recent studies have showed electrochemical HER using acetic acid (AcOH), an even weaker acid ($pK_{a,\ AcOH}$ = 23.51 in MeCN)[46] than $[(DMF)H]^+$ and anilinium in MeCN. For example, a Ni^{II} complex with a N2P2 coordinating ligand (6-((diphenylphosphino)-methyl)pyridin-2-amine) exhibited HER with a TOF of 8400 sec^{-1} at ≥290 mM of AcOH, albeit at a high overpotential,

590 mV.[48] By contrast, a [NiFe]-hydrogenase inspired dithiolate-ligated Ni complex performed electrochemical HER at much lower overpotential, 265 mV. in the presence of low AcOH concentration, ≤50 mM in tetrahydrofuran (THF; $pK_{a,\,AcOH} = 22.48$ in THF)[49], but at comparatively low TOF, 1240 s^{-1}.[9]

Rationale and catalyst design. Based on the [NiFe] hydrogenase and the molecular electrocatalysts discussed above, we focused on three general features when designing new HER catalysts: (1) inexpensive catalysts consisting of earth-abundant transition metal(s) (e.g., Ni), (2) structural and electronic flexibilities at the catalyst's active site to attain different coordination geometries during the catalysis, as seen for the Ni-SI_a, Ni-R, and Ni-C states in [NiFe] hydrogenases, and (3) the presence of a pendant weak Brönsted acid/base to deliver the H^+ toward the metal center at the active site.[50] Based on these features, we have designed two ligands containing S, N, and C atom donors, 3,7-dithia-1,5(2,6)-dipyridinacyclooctaphane (N2S2) and 3,7-dithia-1(2,6)-pyridina-5(1,3)-benzenacyclooctaphane (NCHS2), and herein we report the synthesis and detailed characterization their corresponding Ni^{II} complexes $[(N2S2)Ni(MeCN)_2](OTf)_2$, **1•(OTf)$_2$**, and $(NCHS2)Ni(OTf)_2$, **2**, respectively (Scheme 2). The

two ligands N2S2 and NCHS2 also bear pyridyl group(s) that could be involved in proton binding, similar to the terminal Cys residues in [NiFe] hydrogenases.

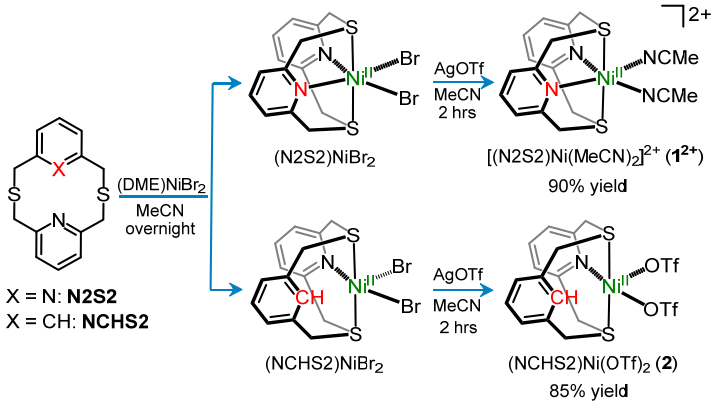

Scheme 2. Synthesis routes outlined for $[(N2S2)Ni(MeCN)_2]^{2+}$ ($\mathbf{1}^{2+}$) and $(NCHS2)Ni(OTf)_2$ (**2**)

We have performed electrochemical HER in MeCN and both $\mathbf{1}^{2+}$ and **2** show high catalytic current, ~15 mA/cm^2, for proton reduction in the presence of a low concentration (≤0.043 M) of trifluoroacetic acid (TFA, pK_a = 12.65 in MeCN),[46,51] in MeCN with ≥1 M of added H_2O. Furthermore, comparative electrochemical activities tested using both Ni^{II} complexes in the presence of AcOH showed that **2** is also an active HER electrocatalyst with TOF_{max}, ~2,000 sec^{-1} at minimal acid concentration, ≤0.05 M, whereas the HER electrocatalysis is convoluted by the background contribution when $\mathbf{1}^{2+}$ was investigated under the identical electrochemical conditions. The electrochemical mechanism investigated for HER using $\mathbf{1}^{2+}$ and **2** indicates that $\mathbf{1}^{2+}$ undergoes two consecutive electro-reduction events first to generate a Ni^0 species that mediated the HER process. In contrast, the **2** follows an electrochemical ECEC mechanism selectively where, E and C indicate the electron and proton transfer process, respectively, with the onset potential for the H^+ reduction near the potential where $Ni^{II/I}$ couple occurs. Interestingly, **2** gets converted into an organometallic complex after the first EC step that further eventually achieves a Ni^{III} species which

sets the platform for the proton reduction process, as similarly observed for HER performed by [NiFe] hydrogenases (Scheme 1). Electron paramagnetic resonance (EPR) spectroscopy was used to detect both Ni^{I} and Ni^{III} species, further supporting our proposed HER mechanism for **2**. In addition, the kinetic properties of our two Ni^{II} electrocatalysts for the HER process in the presence of H_2O have been investigated and benchmarked in comparison with the previously reported molecular HER catalysts.

RESULTS AND DISCUSSION

Syntheses and characterization

N2S2 was synthesized following a slightly modified literature procedure[52] and obtained as white solids with 56% yield. Using a similar synthetic approach, NCHS2 was also prepared by refluxing equivalent moles of 1,3-bis(bromomethyl)benzene and synthetically prepared 2,6-pyridinedimethanethiol in a mixture of 1:1 (v/v) benzene and ethanol for 5 hours, to generate NCHS2 in a 64% yield.[53] The Ni complexes **1•(OTf)$_2$** and **2** were then synthesized following different methods and using (DME)$NiBr_2$ and either N2S2 or NCHS2 as precurors, respectively (Scheme 2). The addition of 2 equiv AgOTf yielded the desired metal complexes **1•(OTf)$_2$** as a purple solid and **2** as a green solid in 90% and 85% yield, respectively. Notably, both **1•(OTf)$_2$** and **2** can be synthesized in a one-step procedure by reacting N2S2 or NCHS2 with 1 equiv of $Ni(OTf)_2$ in MeCN and toluene, respectively, although slightly lower yields of **1•(OTf)$_2$** and **2** were obtained (82% and 60%, respectively).[53]

X-ray crystal structures of **1•(OTf)$_2$** reveals pseudo-octahedral coordination at the Ni^{II} center in a κ^4 conformation, with the two N atoms of the N2S2 ligand and the two MeCN molecules occupy the equatorial positions with an average Ni-N bond distance of 2.06 Å (Figure 1a). In

addition, the two S atoms of N2S2 occupy the axial positions with comparatively longer average Ni-S bond lengths of 2.386 Å. By comparison, the X-ray structure analysis of **2** (Figure 1b) reveals a distorted square pyramidal geometry with a τ_5 value of 0.204,[54] with one OTf ligand found in the axial position, while the other OTf ligand and the N atom and 2 S atoms of NCHS2 occupy the equatorial positions (Figure 1b). The distance between the Ni center and the *ipso* C1 atom of the benzene ring is 2.407 Å, which is considerably shorter than other metal–C distances of similar complexes bearing a similar ligand framework.[55] Interestingly, a metal-arene interaction was observed for **2** in which the Ni1–C1 and Ni1–H1 distances, 2.478 Å and 2.299 Å, respectively along with the Ni1–H1–C1 angle of 89.61° indicate an agostic interaction between the Ni and C_{ipso}–H bond, in line with what was observed previously for related pyridinophane Ni complexes.[55] However, X-ray diffraction studies showed that $\mathbf{1}^{2+}$ adopts an octahedral structure, whereas a square pyramidal geometry was observed for **2** (Figure 1).

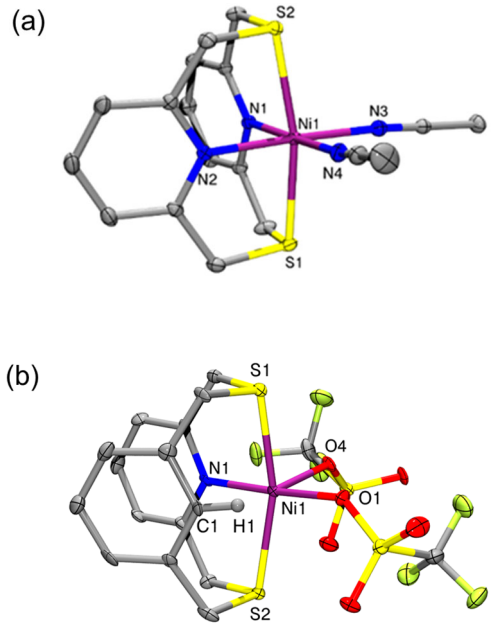

Figure 1. ORTEP representations (50% probability ellipsoids) for (a) the cation of **1•(OTf)$_2$** and (b) **2**. Selected bond distances (Å) and angles (deg°) for $\mathbf{1}^{2+}$: Ni1–N1 2.071(9), Ni1–N2 2.060(10), Ni1–S1 2.379(3), Ni1–S2 2.394(3), Ni1–N3 2.060(10), Ni1–N4 2.039(10), and for **2**: Ni1–N1

2.001(6), Ni1–O4 2.039(5), Ni1–O1 2.043(4), Ni1–S1 2.391(2), Ni1–S2 2.407(2), Ni1–C1 2.478(8), N1–H1 2.299, N1–H1–C1 89.61.

Electrochemical studies

Cyclic voltammetry under N_2-atmosphere

The cyclic voltammogram (CV) of $\mathbf{1}^{2+}$ was first recorded in N_2-saturated 0.1 M $TBAPF_6$ MeCN solution and a quasi-reversible redox wave centered at –1.30 V vs. $Fc^{+/0}$ and an irreversible wave at –1.75 V vs. $Fc^{+/0}$ was observed that can be assigned as $Ni^{II/I}$ and $Ni^{I/0}$ redox couples, respectively (Figure 2a). In addition, a small redox wave at –0.32 V was observed as an oxidative peak, and the origin of this peak might be attributed to the oxidation of surface adsorbed Ni^{I} or Ni^{0} species after being formed in the forward scan reactions. CVs were also collected for $\mathbf{1}^{2+}$ in N_2-saturated MeCN at different scan rates (0.05 V/s – 1.0 V/s) and showed a linear correlation between the cathodic peak currents at the $Ni^{II/I}$ redox couple and the square root of the scan rate, indicating a diffusion-controlled electrochemical processes (Figures S10 and S11).[56]

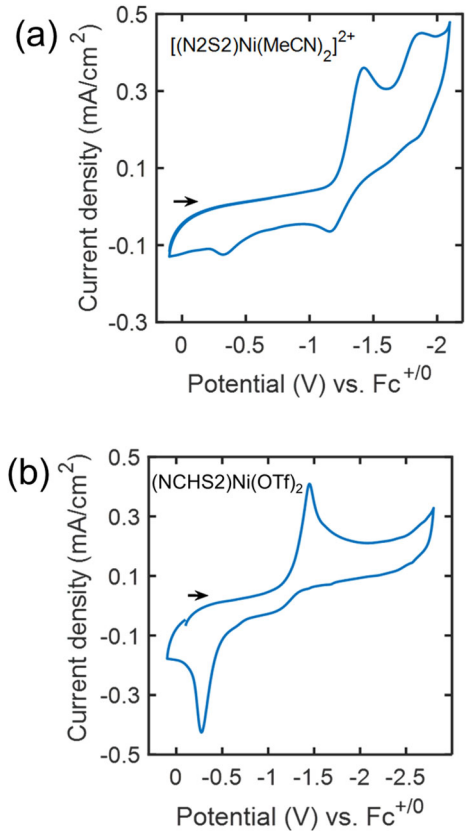

Figure 2. CVs recorded for (a) $\mathbf{1}^{2+}$ and (b) **2** in N_2-saturated 0.1 M $TBAPF_6$ MeCN solution at 0.1 V/s scan rate. The arrow shown in the figures indicates the direction of the scan.

The CVs performed for **2** exhibited a different electrochemical behavior than that of $\mathbf{1}^{2+}$. In N_2-saturated MeCN electrolyte, CVs for **2** showed a single reductive wave at –1.5 ($\pm$0.17) V vs. $Fc^{+/0}$ in the forward scan and an anodic wave around –0.26 $\pm$0.15 V vs. $Fc^{+/0}$ in the reverse scan with similar peak current densities at both waves (Figure 2b). This redox behavior for **2** suggests that the process in the forward scan could be due to the reduction of Ni^{II} to Ni^{I}, yet the corresponding oxidation occurred at a large peak separation, ΔE_p = 1.24 V, when the direction of the CV scan was reversed. Interestingly, when multiple subsequent CV sweeps for **2** in the N_2-saturated MeCN were recorded, a significant shift of the $Ni^{II/I}$ reductive peak potential toward more positive potentials (approximately +0.2 V after ninth CV cycle) was observed (Figure 3). The change in peak positions for **2** with a slight decrease in peak current densities could be an

indication of the structural modification within the metal complex during repeating CV cycles under N_2. Similarly, when the direction of CVs was reversed after completing the cathodic scan, the anodic peak potential at –0.26 V vs. $Fc^{+/0}$ for **2** moved toward lower potentials while scanning repeating CV cycles in N_2-sparged MeCN electrolyte (Figure S18). Such electrochemical behavior could be due to chemical reactions or rearrangement in the metal coordination environment for **2** during the successive CV sweeps.

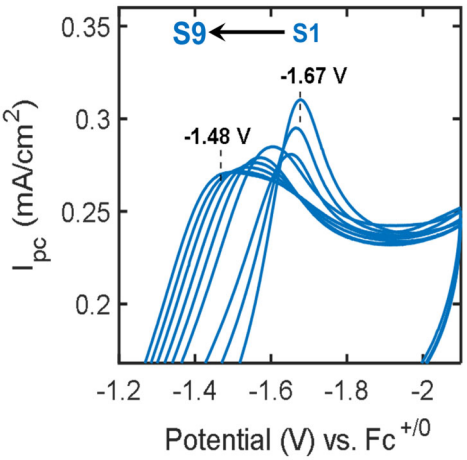

Figure 3. CVs for **2** in N_2-saturated 0.1 M $TBAPF_6$ MeCN upon nine repeating CV sweeps. S1 and S9 indicate the first and ninth CV sweeps, and the black arrow shows the direction of the peak shift. Only reductive waves for $Ni^{II/I}$ redox couples are shown for clarity.

Further studies were carried out by recording CVs at different scan rates for **2** in the N_2-saturated MeCN (Figure 4a), and peak current densities at $Ni^{II/I}$ reductive wave maintained linear correlation with the square root of scan rate (Figure S21). The shift in peak potentials at $Ni^{II/I}$ reduction wave at different scan rates showed a linear dependence of 61 mV per decade (Figure 4b) that suggests a Nernstian electron transfer step (E) for **2**, followed by a chemical process (C).[57-59]

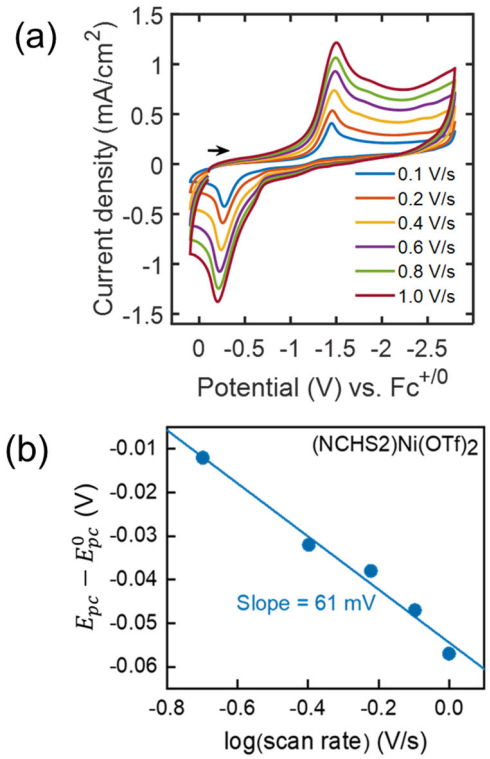

Figure 4. (a) CVs recorded for **2** in N_2-saturated 0.1 M $TBAPF_6$ MeCN at different scan rates (0.1 V/s – 1 V/s). (b) Peak shifts at $Ni^{II/I}$ reductive waves obtained from (a) at different scan rates are plotted versus the logarithm of scan rates (V/s). E^0_{pc} is the potential observed at the $Ni^{II/I}$ reductive wave at 0.1 V/s scan rate. The R^2 value for the linear fit is 0.98.

Accounting for the key features presented above, an overall electrochemical EC process involving a single e^- and single H^+ transfer for **2** under N_2 inert atmosphere can be proposed as outlined in Scheme 3. Is it expected that **2** converts into $[(NCHS2)Ni(MeCN)_2]^{2+}$ ($\mathbf{2}^{2+}$) upon dissolution into MeCN, and the electrochemical events start with a single e^- reduction of $\mathbf{2}^{2+}$ to form $\mathbf{2}^+$, which could undergo either a concerted metalation-deprotonation step[60] to form a square planar complex **3**, or an oxidative addition process to form a Ni^{III}–H species, **4**. Overall, this suggess that that the first Ni^{II}-to-Ni^{I} electroreduction process for $\mathbf{2}^{2+}$ is coupled with the activation of the nearest C–H bond of the coordinating NCHS2 ligand to generate **3**. Interestingly, complex **3** resembles the Ni center in the Ni-L state (Scheme 1), where the pendant pyridinium residue in **3** could act as like protonated terminal Cys residue in [NiFe] hydrogenases. When the direction of

the forward scan is reversed, **3** could get oxidized to form $[(NCS2)Ni(MeCN)_2]^+$ (**5**), which can then be further reduced by a single e^- and a single H^+ to yielde **3**. Thus, regeneration of $\mathbf{2}^+$ from **5** under N_2 atmosphere could be inhibited after successive electrochemical EC processes in the absence of added protons, and hence results in the movement at the peak potentials upon subsequent CV sweeps (Figure 3). In addition, these redox events also induce a change in the metal-ligand coordination and the associated reorganization energy between the square planar complex **3** and the octahedral species **5** causes the large peak separation in the CVs recorded for $\mathbf{2}^{2+}$ (Figure 2b), which formed upon dissolution of **2** in N_2-saturated MeCN..

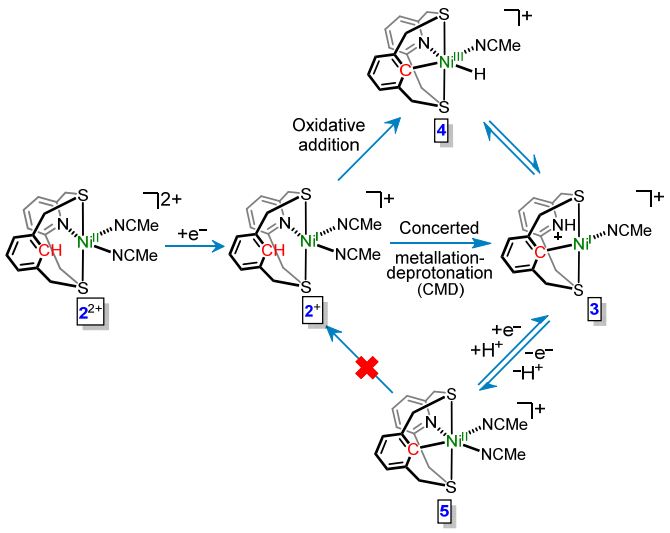

Scheme 3. Proposed electrochemical events for $\mathbf{2}^{2+}$ in the N_2-saturated dry MeCN electrolyte.

To further benchmark our proposed electrochemical mechanism, as shown in Scheme 3, we synthesized complex **5** independently in a two-step procedure, starting with the NCBrS2 ligand and $Ni(COD)_2$ (Scheme 4).[53] Single crystal X-ray crystallography of the reaction mixture reveals a dinuclear complex, $[(NCS2)Ni(\mu\text{-}Br)]_2$ (**5'**, Figure 5), which is a possible intermediate that could yield **5** upon halide elimination using AgOTf.[53] The distance between two Ni centers in **5'** was found to be 3.869 Å, with no significant bonding interaction between the Ni atoms. The

coordination geometry of both Ni centers is distorted octahedral, with two S atoms in the axial positions and the ligand binding in a κ^4 conformation. While the bond distance between Ni–N1 (2.042 Å) and Ni–S (average 2.383 Å) are comparable to those of $\mathbf{1}^{2+}$ and **2**, the Ni-C1 distance is significantly shorter than that in **2** (1.980 Å vs. 2.478 Å. Figure 5), as expected for the presence of a bonding interaction, and in agreement with those observed for other similar organometallic Ni complexes.[61]

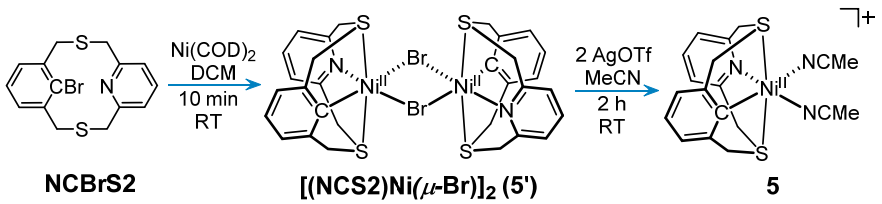

Scheme 4. The synthesis of complexes **5'** and **5**.

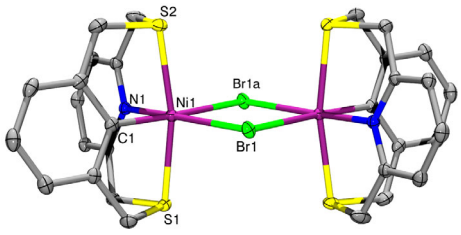

Figure 5. ORTEP representations (50% probability ellipsoids) of **5'**. Selected bond distances (Å): Ni–N1 2.042(1), Ni–C1 1.980(1), Ni–S1 2.3759(5), Ni–S2 2.3899(5), Ni–Br1 2.5487(4), Ni–Br1a 2.720(4).

However, we hypothesized that the reduction potential for the Ni^{II} to Ni^{I} center of **5** will be higher than that of $\mathbf{2}^{2+}$. The CV obtained for **5** in N_2-saturated MeCN showed a redox wave for the $Ni^{II/I}$ reduction process at –1.31 V vs. $Fc^{+/0}$ (first CV sweep; S1 in Figure 6) that is at least 0.35 V more positive than that of **2**. Interestingly, repeating CV sweeps recorded for **5** (Figure 6) showed degradation at the peak currents for the Ni^{II} to Ni^{I} redox process, and the peak potentials moved toward more negative potentials, in the opposite direction of movement to that observed for **2** (Figure 3). Such degradation in peak current densities observed for **5** could be attributed as

the dissociation of the Ni–C bond upon reduction and thus results the formation $\mathbf{2}^{2+}$ in the presence of residual protons that causes the movement of $Ni^{II/I}$ peak potential toward more negative potentials while recording subsequent CV cycles. Noteworthy, the reduction potential for the $Ni^{II/I}$ redox process observed for **5** after the fourth CV cycle appeared at –1.64 V vs. $Fc^{+/0}$ that matches the cathodic peak potential of the first CV sweep obtained for **2** (Figure 3). Overall, these data support our hypothesis for the conversion between complexes **2** and **5** under reducing electrochemical conditions.

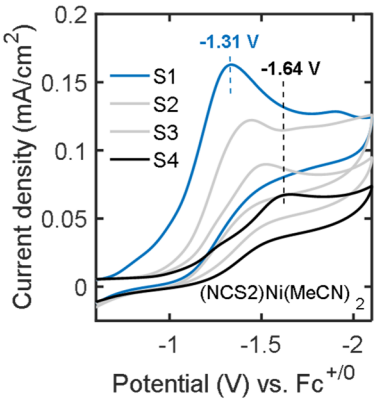

Figure 6. CVs recorded for **5** in N_2-saturated 0.1 M $TBAPF_6$ MeCN upon four repeating CV sweeps. S1 (blue) and S4 (black) indicate the first and fourth CV sweeps. Only reductive waves for $Ni^{II/I}$ redox couples are shown for clarity.

We have also employed EPR spectroscopy to further support our proposed redox properties of **2**. When complex **2** was reduced using one equiv of $Co^{II}Cp_2$ (Cp = cyclopentadienyl), the EPR spectrum in 1:3 MeCN:PrCN (v/v) at 77 K reveal a pseudo-axial signal that closely matches the EPR signal obtained when **5** was reduced with the same chemical reductant (Figure 7). For both the cases, EPR signals revealed an axial pattern with the *g* values; $g_x = 2.246$, $g_y = 2.202$, and $g_z = 2.008$ ($A_{2N} = 11$ G). We attribute such EPR data as the formation of Ni^{I} species, most likely complex **3** that could be prepared by reducing **2** (or $\mathbf{2}^{2+}$), as well as upon reducing **5** that could get protonated by residual protons.

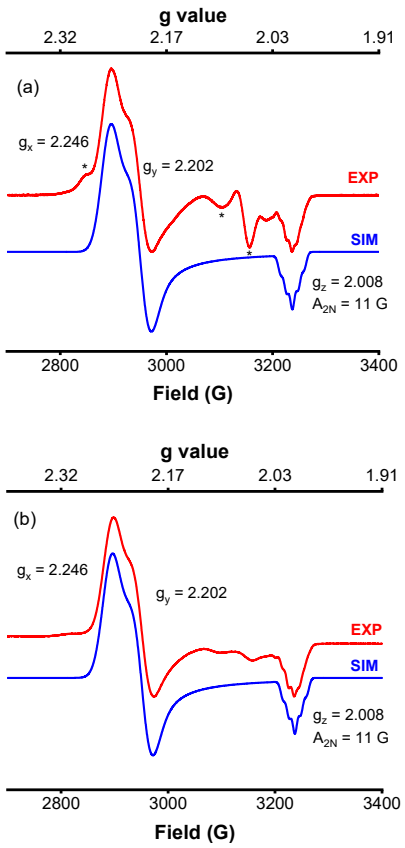

Figure 7. Experimental (red) and simulated (blue) EPR spectra for the mixture of (a) **2** and (b) **5** with $Co^{II}Cp_2$ present in the solution of MeCN/PrCN (1:3) at 77 K. The features marked with * correspond to unknown.

Cyclic voltammetry in the presence of CH_3COOH (AcOH)

CVs were carried out for $\mathbf{1}^{2+}$ and **2** in N_2-sparged 0.1 M $TBAPF_6$ MeCN solution in the presence of a different amount of AcOH. Addition of AcOH into MeCN electrolyte containing $\mathbf{1}^{2+}$ showed an increase in current densities with onset potential near $Ni^{I/0}$ redox couple, and quasi-plateau current beyond –2.0 V vs. $Fc^{+/0}$ remained increasing as the concentration of AcOH was increased (Figure S13). However, the direct reduction of AcOH by glass carbon electrode overlaps with the catalytic currents observed for $\mathbf{1}^{2+}$ within the chosen electrochemical window (Figure S31). On the contrary, the catalytic peak current for $\mathbf{2}^{2+}$ after the addition of a similar amount of AcOH as used for $\mathbf{1}^{2+}$ in the N_2-saturated MeCN appeared at 140 mV more positive potential than

that of direct proton reduction by GC electrode (Figure S31). Additionally, $\mathbf{2}^{2+}$ exhibited an interesting pre-catalytic wave prior to $Ni^{II/I}$ redox couple, around –1 V vs. $Fc^{+/0}$ that shifted toward more positive potentials with increasing the concentrations of AcOH in the electrolyte solution (Figure 8). Such pre-catalytic waves are typically observed for multi-H^+ and multi-e^- reactions when an electrochemically stable intermediate exists prior to the electrocatalysis process.[62,63] Noteworthy, no such pre-catalytic wave was observed for $\mathbf{1}^{2+}$ after the addition of AcOH under the identical electrochemical conditions.

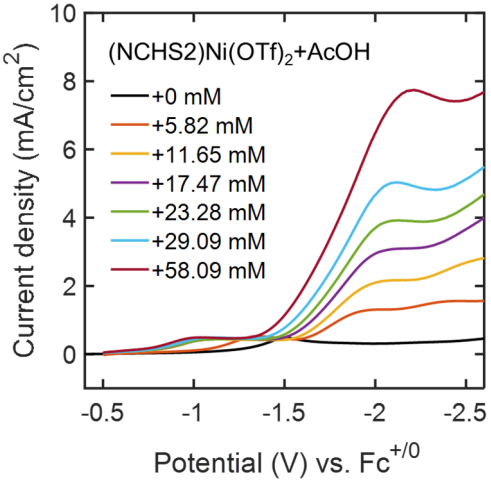

Figure 8. CVs collected for **2** in N_2-saturated 0.1 M $TBAPF_6$ MeCN solution in the absence (back) and the presence of different concentrations of AcOH (5.82 mM - 58.09 mM) as shown in the legend. All CVs were recorded at 0.1 V/s scan rate. Only forward scans are shown for clarity.

Cyclic voltammetry in the presence of CF_3COOH (TFA)

The effect of a comparatively stronger acid than AcOH in MeCN toward electrochemical HER was also tested by choosing TFA. CVs were first recorded by dissolving only TFA at different acid concentrations (0 M to 0.043 M) in 0.1 M $TBAPF_6$ MeCN to benchmark the background proton reduction by using a GC electrode (Figure S5). TFA showed two irreversible redox waves at –1.7 V and –2.25 V vs. $Fc^{+/0}$ in the forward scan, as expected for a conjugate base of a strong acid that could undergo homoconjugation process upon dissociation.[46] An increase in

TFA concentration in the MeCN electrolyte moved the peak potentials of those redox waves slightly toward higher potentials (Figure S5).

CVs collected for $\mathbf{1}^{2+}$ in MeCN at different concentrations of TFA showed catalytic currents with two redox waves at potentials lower than –1.0 V vs. $Fc^{+/0}$ (Figure S12), where the second redox wave after the $Ni^{I/0}$ potential exhibited larger current densities and the peak potentials of both redox waves moved toward more negative potential as the concentration of TFA increases. These results suggest a higher degree of proton reduction mostly around the potential of $Ni^{I/0}$ couple for $\mathbf{1}^{2+}$ in the MeCN electrolyte. However, similar electrocatalytic improvement in current densities was also observed for $\mathbf{2}^{2+}$ in the presence of TFA (Figure 9a). Interestingly, the onset of the catalytic current at different concentrations of TFA is more positive than the potential of $Ni^{II/I}$ redox couple for $\mathbf{2}^{2+}$, but the peak currents appeared after the $Ni^{II/I}$ redox potential, indicating the occurrence of proton reduction based on the electrochemically generated Ni^{I} center in MeCN. These results propose a different electrochemical mechanism for HER using $\mathbf{2}^{2+}$, compared to $\mathbf{1}^{2+}$ or other Ni^{II}-based HER electrocatalysts in the literature that perform proton reduction based on electrochemically generated Ni^{0} center.[45,47,64]

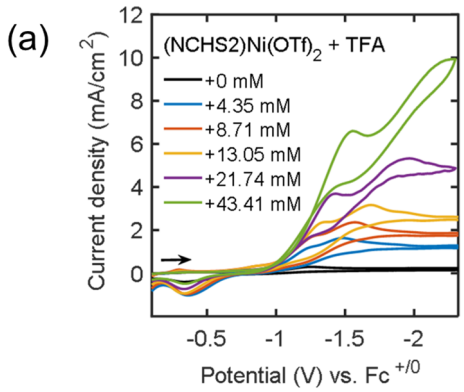

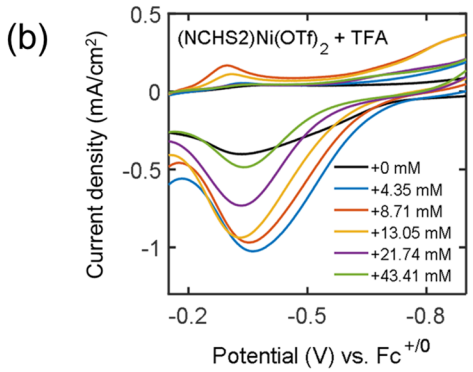

Figure 9. (a) CVs collected for $\mathbf{2}^{2+}$ in N_2-saturated 0.1 M $TBAPF_6$ MeCN solution in the absence (back) and the presence of different concentrations of TFA (4.35 mM – 43.41 mM) as shown in the legend. (b) Same as (a), but the electrochemical window between –0.2 V and –0.8 V vs. $Fc^{+/0}$ is magnified. All CVs were recorded at 0.1 V/s scan rate.

At the same concentration of TFA (0.043 M) in the MeCN solution, CVs collected for $\mathbf{1}^{2+}$ and $\mathbf{2}^{2+}$ showed similar current densities, but the peak potentials at the catalytic waves are at least 365 mV more positive than that of direct proton reduction by GC working electrode using the identical amount of TFA in the absence of a catalyst (Figure S32). Although both catalysts exhibited a similar degree of proton reduction in MeCN electrolyte in the presence of an identical amount of TFA, CVs carried out for $\mathbf{2}^{2+}$ showed interesting redox behavior at different concentrations of added TFA while scanning oxidatively after completing the cathodic scan. $\mathbf{2}^{2+}$ showed a redox wave around –0.3 V vs. $Fc^{+/0}$ with peak current density ~1 mA/cm^2 in the presence of 0.043 M of TFA in the MeCN electrolyte that gradually decreased as the concentration of TFA was increased in the electrolyte solution (Figure 9b). The significance of these redox features observed for $\mathbf{2}^{2+}$ in the presence of a stronger acid in MeCN could be important for proposing a mechanistic outline for HER.

Proposed mechanism

Based on the catalytic currents observed for $\mathbf{1}^{2+}$ at potentials lower than the reduction potential of the $Ni^{I/0}$ process, we propose a typical $E_1E_2C_1C_2$ electrochemical mechanism (Scheme

5, left) for $\mathbf{1}^{2+}$ that follows two sequential e^- reduction of the Ni^{II} complex first to yield Ni^0 derivative which undergoes next two consecutive H^+ reduction process for H_2 evolution, as commonly seen for the Ni^{II}-based HER electrocatalysts.[45,47] However, the electrochemical mechanism for HER is different when $\mathbf{2}^{2+}$ was used homogeneously in the MeCN electrolyte in the presence of different organic acids, e.g., AcOH, TFA, etc. An overall outline for electrochemical HER mechanism using $\mathbf{2}^{2+}$ is proposed herein (Scheme 5, right). We anticipate that **3** is most likely to be in equilibrium with **4** after being formed from $\mathbf{2}^{2+}$ through an overall EC process, as shown in Scheme 3. While scanning reductively in the forward CV scan, **4** also could get reduced by $1e^-$ to generate a Ni^{II}-hydride species (**6**), which is a common intermediate observed for molecular HER electrocatalysts promoted by Ni^{II} complexes[45,47], as similarly anticipated for the $\mathbf{1}^{2+}$ ($\mathbf{1\text{-}H}^+$) after the $E_1E_2C_1$ steps. In regards, we also account the possible $E_1C_1'E_2'$ process for $\mathbf{1}^{2+}$ to yield such hydride species, $\mathbf{1\text{-}H}^+$ (Scheme 5, left, dotted line), as a small amount of current enhancement was observed for $\mathbf{1}^{2+}$ around the $Ni^{II/I}$ reduction potential in the presence of acids (Figure S12 and S13). Therefore, we propose a mixture of electrochemical mechanisms; $E_1E_2C_1C_2$ (major pathway) and $E_1C_1'E_2'C_2$ (minor pathway) for $\mathbf{1}^{2+}$ toward H_2 evolution catalysis, as seen in the literature.[47] However, **2** (or $\mathbf{2}^{2+}$) follows selective $E_1C_1E_2C_2$ mechanistic pathway as subsequent $2e^-$ reduction of Ni^{II} center to generate Ni^0 center is not favorable (Scheme 3).

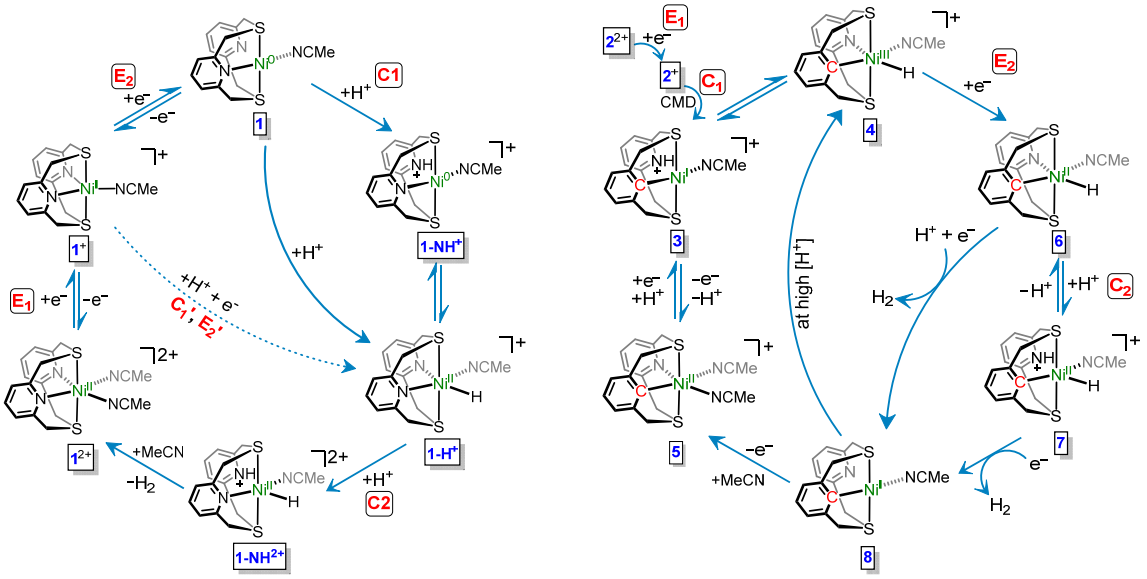

Scheme 5. Proposed electrochemical HER mechanisms promoted by $\mathbf{1}^{2+}$ (left) and $\mathbf{2}^{2+}$ (right), respectively. CMD indicates a concerted metalation deprotonation step as shown in Scheme 3.

However, the further reduction of Ni-hydride species, **1-H**$^{+}$ (for $\mathbf{1}^{2+}$) and **6** (for $\mathbf{2}^{2+}$) to release H_2 as the product requires either direct protonation at the Ni-hydride species or via protonation of the pendant pyridyl group of the coordinating ligand, N2S2 and NCHS2, respectively. CVs recorded for $\mathbf{2}^{2+}$ in the presence of AcOH in the MeCN solution showed a prominent pre-catalytic wave prior to the $Ni^{II/I}$ reductive wave (Figure 8) that could be associated with the formation of an electrochemically stable intermediate, **7** upon protonation of the pyridyl-N in coordinating NCHS2 ligand. Such complex **7** then can release H_2 at the more reducing condition as the CV was scanned toward more negative potential than the reduction potential for the $Ni^{II/I}$ couple. In contrast, in the presence of TFA, a comparatively stronger acid than AcOH did not exhibit any such pre-catalytic wave for $\mathbf{2}^{2+}$, but the onsets of the catalytic current lie at more positive potentials than the reduction potential of $Ni^{II/I}$ (Figure 9a). It is likely that **6** will undergo faster proton reduction events in the presence of a stronger acid (such as TFA) while CV was scanned toward more reducing conditions and yield **8** after releasing H_2. Thus, the stabilization of

any such intermediate like **7** is less likely to be captured, and hence, the pre-catalytic wave was not found for $\mathbf{2}^{2+}$ in the presence of TFA. On the other hand, the release of H_2 from the intermediate $\mathbf{1\text{-}H}^{+}$ also could involve a protonation step of the pyridyl group of the chelating N2S2 ligand and yield intermediate, $\mathbf{1\text{-}NH}^{2+}$.

Finally, after completing the successive HER in the reductive scan in a CV, when the direction of the CV was reversed, a new anodic redox wave at –0.3 V vs. $Fc^{+/0}$ was observed for $\mathbf{2}^{2+}$ in the presence of TFA, and the peak current decreased as the concentration of the TFA was increased in the MeCN electrolyte (Figure 9b). Such electrochemical behavior can be interpreted as the oxidation of **8** to **5**, but at the high TFA concentrations it is also expected that **8** could abstract a H^+ from the bulk solution and regenerate **4**. Therefore, the rate of formation for **5** from **8** becomes slow, and hence the peak current densities at the anodic wave around –0.3 V degraded at the higher TFA concentration. However, **5** can be further reduced by $1H^+$ and $1e^-$ to obtain **3** (Scheme 3), and thus **3** can reenter the catalytic cycle.

Overall, it is interesting that **2** (or $\mathbf{2}^{2+}$) follows a very selective ECEC type electrochemical mechanism for HER, in which the $[Ni^{III}H]$ species could be a potential intermediate as similarly observed for [NiFe] hydrogenases in the Ni-C state.[10] Herein, our attempts to oxidize $\mathbf{1}^{2+}$ and **2** to achieve their corresponding Ni^{III} complexes were not successful using $NOPF_6$ as a chemical oxidant, which could be because of the high redox potentials of the $Ni^{II/III}$ oxidation process of +1.5 V (Figure S16) and +1.2 V (Figure S27) vs. $Fc^{+/0}$, respectively. However, the electrocatalytic behavior of **5** for HER is similar in the presence of TFA as observed for **2** (Table S1 and Figure S29), and hence, we chose complex **5** to probe any potential paramagnetic intermediates via EPR spectroscopy. The EPR spectrum of **5** in 1: 3 MeCN:PrCN (v/v) at 77 K after oxidizing with one equiv of $NOPF_6$ exhibits complex EPR signal pattern (Figure 10a) that can be simulated as a

combination of overlapping signals for two Ni^{III} species. EPR simulations carried out using g_x = 2.173, g_y = 2.08 (A_N = 16 G), and g_z =1.990 support a Ni^{III} species with a rhombic EPR signal, coupled to one ^{14}N (I = 1). Similarly, an axial EPR signal also could be attributed to another Ni^{III} species using the g values as g_z = 2.173, g_x = g_y = 2.04. Although identification of such Ni^{III} species outside of the scope in this work, we speculate that both EPR signals could be due to two different conformers of related Ni^{III} species.

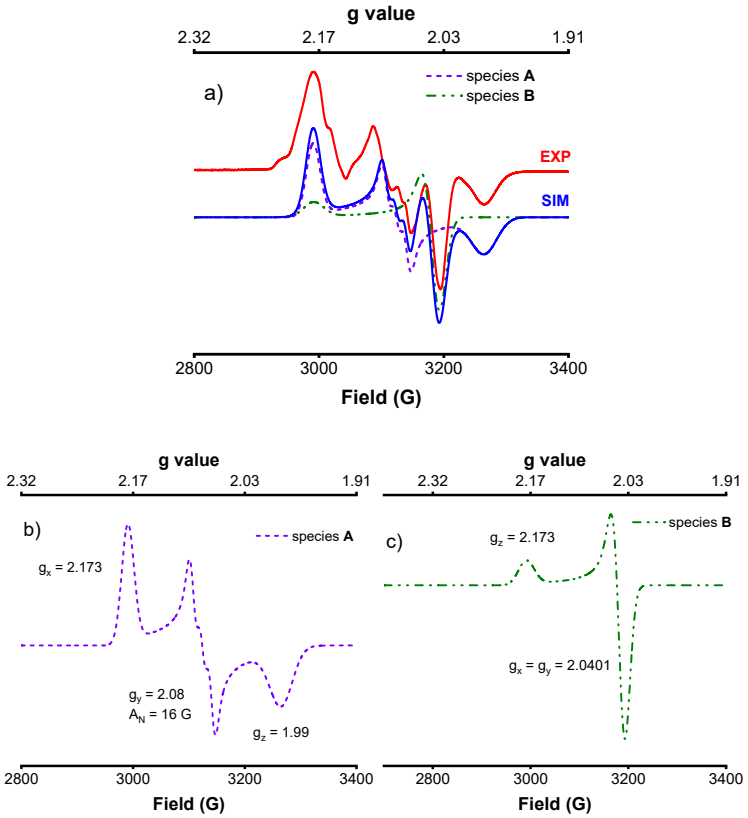

Figure 10. a) Experimental (MeCN:PrCN, 77K) and simulated EPR spectra of **5** + $NOPF_6$. b) and c) The simulated EPR spectra of the two independent species A and B, which are tentatively assigned to Ni^{III} species in two different conformations.

Influence of water on electrochemical HER

Both $\mathbf{1}^{2+}$ and $\mathbf{2}^{2+}$ complexes showed two reductive waves with the catalytic peak currents in the presence of TFA in MeCN electrolyte. The appearance of two reductive waves are expected for a strong acid like TFA as the equivalent amount of its conjugate base can undergo homoconjugation process with the parent TFA.[46] The addition of water is known to hinder such homoconjugation processes[45,46] and hence, show only a single reductive wave in the CV (Figure S6). Furthermore, the addition of water also can improve the availability of the proton source in the organic electrolyte that could enhance the reaction kinetics without compromising the thermodynamic limitations (e.g., changing the redox potential or applied overpotential).

In the CVs recorded for $\mathbf{2}^{2+}$, quasi-plateau currents were observed at potentials lower than –1.5 V vs. $Fc^{+/0}$ in the MeCN electrolyte in the presence of 0.043 M of TFA and 0.8 M of H_2O (Figure 11a). Although the presence of such amount of H_2O in the MeCN + 0.043 M TFA did not have a large effect on the onset potential and the peak current compared to the CV recorded for $\mathbf{2}^{2+}$ in the absence of H_2O, the addition of more than 0.8 M of H_2O showed an increase in the plateau-current densities (Figure 11a). While $\mathbf{2}^{2+}$ is also an active HER electrocatalyst in the presence of AcOH, the peak current densities achieved at low AcOH concentration (0.058 M) is ~50% lower than that of observed for the same catalyst by using 0.043 M of TFA. Interestingly, the CVs recorded for $\mathbf{2}^{2+}$ after the addition of H_2O up to 2.6 M in MeCN containing 0.058 M of AcOH showed comparable peak current densities as observed for the same catalyst when 0.043 M of TFA was used with ≤2 M of added H_2O in the non-aqueous solution (Figure 11b). Together, these results suggest that $\mathbf{2}^{2+}$ sets a new example of catalysts that is efficient enough to perform HER at a very low acid concentration using a moderate to weak acid in wet MeCN. However, similar results were also obtained for $\mathbf{1}^{2+}$ in the presence of H_2O in acid containing MeCN after performing the same set of electrochemical experiments (Figures S14 and S15).

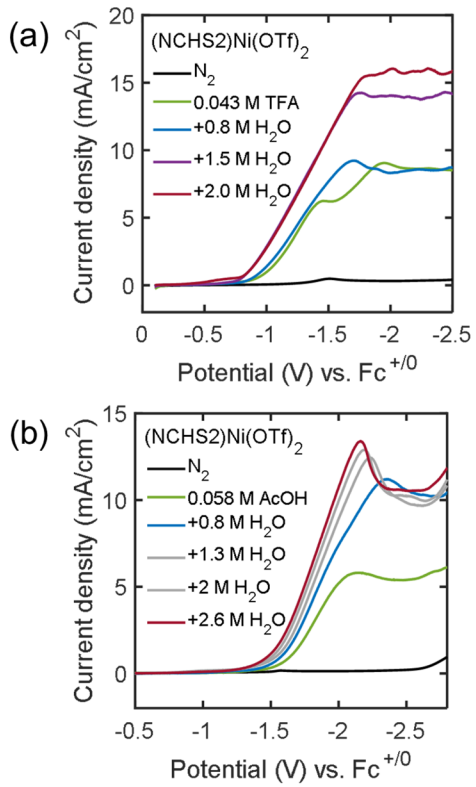

Figure 11. Linear sweep voltammograms for $\mathbf{2}^{2+}$ recorded in N_2-saturated 0.1 M $TBAPF_6$ MeCN in the absence of acid (black) and the presence of (a) 0.043 M TFA and (b) 0.058 M AcOH at different H_2O concentration (as mentioned in the figures legends) added in the electrolyte. Scan rate = 0.1 V/s.

Kinetic insights and catalytic Tafel plots

Kinetic insights for $\mathbf{2}^{2+}$ were gained through the foot-of-the-wave analysis (FOWA), considering that $\mathbf{2}^{2+}$ follows an electrochemical ECEC mechanism in general for HER and there is no catalysts degradation or substrate depletion during the purely diffusion-controlled electrochemical reactions.[65,66] The slopes obtained from the linear fit at the lower range of $[1+\exp(f(E-E_{1/2})]^{-1}$ of such FOWAs; where f = 38.94 V^{-1}, E is the applied potential, and $E_{1/2}$ is the potential for $Ni^{II/I}$ redox couple, provided similar pseudo-first-order rate constants (k_{FOWA}) by using $\mathbf{2}^{2+}$ at the different concentrations of added H_2O, 0.8 M, 1.5 M, and 2 M in the MeCN electrolyte+0.043 M TFA (Figure S35). Under these electrochemical conditions, the average value of maximum turnover frequency ($TOF_{max} = k_{FOWA}$) was estimated as 5.04($\pm$0.02) $\times$ 10^5 s^{-1} for $\mathbf{2}^{2+}$

that also leads to obtain the overall second-order rate constant, k_1 ($k_1 = k_{FOWA}$ / [H^+]) as 1.17($\pm$0.04) $\times$ 10^7 M^{-1} s^{-1} (Table S3). However, the TOF_{max} obtained for $\mathbf{2}^{2+}$ at low concentration of TFA (0.043 M) in the wet MeCN electrolyte is approximately 5-fold and 100-fold larger than the literature known $[Ni(P^{Ph}_2N^{Ph})_2]^{2+}$ complex[32] or a Ni^{II}-complex chelating 1-aza-3,7-diphosphacyclooctanes, $(Ni(8P_2N)_2)$[45] respectively. For both, $[Ni(P^{Ph}_2N^{Ph})_2]^{2+}$ and $Ni(8P_2N)_2$ HER electrocatalysts, TOF_{max} were achieved using MeCN with added water (>1 M) in the presence of $[(DMF)H]^+$ which is a comparatively stronger acid than TFA in the MeCN as discussed above. A competitive HER electrocatalyst could be $[Ni(P^{Ph}_2N^{Ph}_2)_2]^{2+}$ in the MeCN electrolyte in the presence of ≥0.6 M of anilinium[47] that shows 8-fold higher TOF_{max} than that of our $\mathbf{2}^{2+}$ in the presence 0.043 M of TFA with ≥0.8 M of added H_2O, but the acidity of anilinium is still slightly higher than TFA in MeCN. Overall, it is impressive that our $\mathbf{2}^{2+}$ exhibits competitively high turnover for the proton reduction at low acid concentrations, ≤0.043 M using a moderately weak organic acid, TFA, with ≥0.8 M of added water in the MeCN electrolyte.

A similar set of kinetic analysis was also carried out for $\mathbf{1}^{2+}$ in the MeCN electrolyte in the presence of 0.043 M of TFA at three different concentrations of H_2O, 1 M, 1.5 M, and 2 M. Under these electrochemical conditions, $\mathbf{1}^{2+}$ also showed plateau currents at the potentials lower than the potential of $Ni^{I/0}$ redox couple, and the plateau currents increased in current densities as the concentration of H_2O was increased (Figure S14). These typical "S-shape" CVs were then fitted using the FOWA equation,[53] and the slope obtained from the linear portion at the lower regime of the foot-of-the-wave was used to extract TOF_{max} values at the above mentioned electrochemical conditions in the presence of different H_2O concentrations (Table S2).[53] However, the average $TOF_{max} = k_{FOWA}$ estimated for $\mathbf{1}^{2+}$ at different concentration of added H_2O was 1.95($\pm$0.01)$\times 10^5$ s^{-1}, which is 2.6-fold lower than that of $\mathbf{2}^{2+}$ for electrochemical proton reduction (Figure 12a). The

overall second-order reaction rate constant, k_1 for $\mathbf{1}^{2+}$, was also calculated and obtained as $4.53(\pm 0.23)\times 10^6\ M^{-1}\ s^{-1}$. Comparative kinetic data as discussed for $\mathbf{1}^{2+}$ and $\mathbf{2}^{2+}$ indicate that $\mathbf{2}^{2+}$ proceeds HER in a faster kinetic pathway compare to the $\mathbf{1}^{2+}$ under the same electrochemical environment. We attribute that such faster kinetics for $\mathbf{2}^{2+}$ toward proton reduction could be because of the protonation at the N atom of the coordinating NCHS2 ligand followed by the C–H bond activation (Scheme 3), that yields **3** which could provide an inner-sphere proton docking site nearer the catalyst's active center and therefore, facilitate the faster proton transfer compare to that of $\mathbf{1}^{2+}$ where the first proton transfer (C_1 step in Scheme 5) for $\mathbf{1}^{2+}$ happens directly from the bulk solution in a diffusion-controlled process.

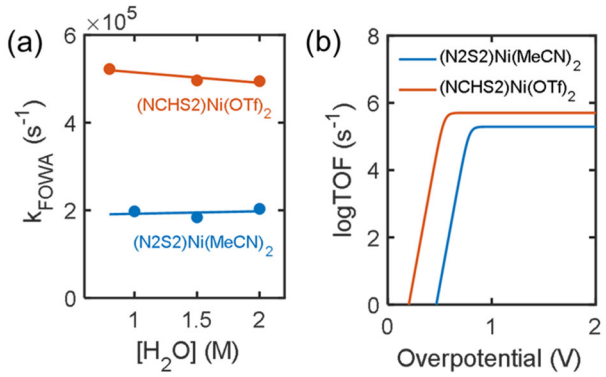

Figure 12. (a) Comparative k_{FOWA} (=TOF_{max}) (s^{-1}) obtained for $\mathbf{1}^{2+}$ and **2** (or $\mathbf{2}^{2+}$) plotted versus different concentrations of added H_2O in 0.1 M $TBAPF_6$ MeCN + 0.043 M TFA solution. (b) Comparative catalytic Tafel plots for $\mathbf{1}^{2+}$ and **2** (or $\mathbf{2}^{2+}$) considering the average TOF_{max} obtained from (a).

The overpotential calculated using the Appel and Helm method[67] for $\mathbf{2}^{2+}$ is 490 mV at $E_{cat/2}$ that is 240 mV lower compare to the $\mathbf{1}^{2+}$ in the presence of 0.043 M TFA with 1.5 M of added water in the MeCN. Under these identical electrochemical conditions, chronoamperometric experiments carried out for $\mathbf{1}^{2+}$ and $\mathbf{2}^{2+}$ showed a similar amount of charge passed, 199 mC and 222 mC, over 15 mins of electrolysis at the applied potential of $E_{cat/2}$ and that correspond to the accumulation of 1.03×10^{-6} moles and 1.15×10^{-6} moles of H_2, respectively (Figure S33). It is

noteworthy that both catalysts exhibited comparatively stable currents during the above chronoamperometric measurements, and the average currents were much higher than the background contribution under the identical electrochemical conditions. However, comparative catalytic Tafel plots for $\mathbf{1}^{2+}$ and $\mathbf{2}^{2+}$ were also constructed using their corresponding average TOF_{max} values as extracted from the FOWA, and it is prominent that $\mathbf{2}^{2+}$ performs proton reduction with higher TOF but at low overpotential than that of $\mathbf{1}^{2+}$ under the same electrochemical circumstances (Figure 12b). Such electrochemical behavior toward HER using $\mathbf{2}^{2+}$ is significantly important since the high turnover usually comes at the high cost of overpotential for molecular catalysis.[9,48] To further benchmark our electrocatalysts, we have compared their catalytic Tafel plots to those of the previously reported Ni^{II} molecular HER electrocatalysts[32,45], such as $[Ni(P_2^{Ph}N^{Ph})_2]^{2+}$ and $Ni(8P_2N)_2$ in the presence of $[(DMF)H]^+$ in wet MeCN electrolyte, or $[Ni(P^{Ph}{}_2N^{Ph}{}_2)_2]^{2+}$ in the presence of anilinium[47], as shown in Figure 13.[53] Our $\mathbf{2}^{2+}$ reduces protons with higher TOF in the presence of 0.043 M of TFA and 1.5 M of H_2O than that of $[Ni(P_2^{Ph}N^{Ph})_2]^{2+}$ and $Ni(8P_2N)_2$ in which ≥0.42 M of $[(DMF)H]^+$ was used as the proton source with ≥1.2 M of added H_2O in MeCN. However, the overpotential associated with $\mathbf{2}^{2+}$ is similar as obtained for $Ni(8P_2N)_2$ but 290 mV lower compared to $[Ni(P_2^{Ph}N^{Ph})_2]^{2+}$, albeit $[(DMF)H]^+$ is stronger acid in the MeCN than TFA. By contrast, the TOF observed for $[Ni(P^{Ph}{}_2N^{Ph}{}_2)_2]^{2+}$ electrocatalyst[47] in MeCN in the presence of ≤0.6 M anilinium shows higher TOF at 350 mV of lower overpotential than that of our $\mathbf{2}^{2+}$ in the presence of 0.043 M TFA with 1.5 M of added H_2O. Moreover, it is noteworthy that our $\mathbf{1}^{2+}$ showed similar electrocatalytic activity for HER as seen for the $[Ni(P_2^{Ph}N^{Ph})_2]^{2+}$ complex[32], where the acidity of the electrolyte solutions used for $\mathbf{1}^{2+}$ was identical as used for $\mathbf{2}^{2+}$ (0.043 M TFA+1.5 M H_2O).

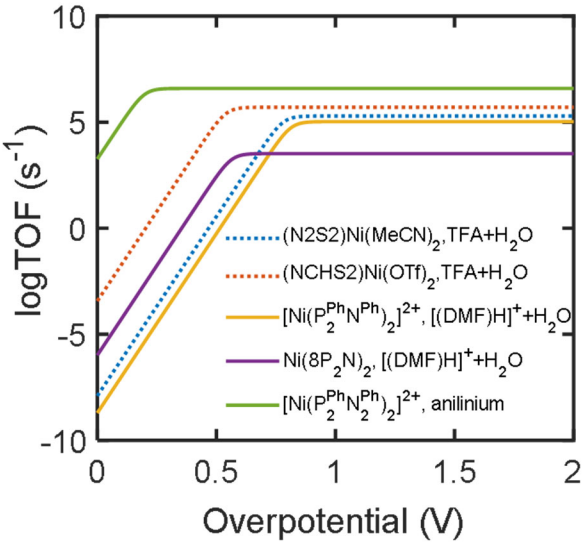

Figure 13. Comparative catalytic Tafel plots for our $\mathbf{2}^{2+}$ (orange, dotted) and $\mathbf{1}^{2+}$ (blue, dotted) in the presence of 0.043 M TFA+1.5 M H_2O, $[Ni(P_2^{Ph}N^{Ph})_2]^{2+}$ (yellow, solid) and $Ni(8P_2N)_2$ (purple, solid) in the presence of $[(DMF)H]^+$(≥0.42 M)+H_2O(≥1.2 M) [32,45], and $[Ni(P_2^{Ph}N_2^{Ph})_2]^{2+}$ in the presence of ≤0.6 M anilinium (green, solid).[47] The electrolyte used for all these experiments is 0.1 M $TBAPF_6$/MeCN. The TOF_{max} for the reported electrocatalysts were taken from their reported values, and overpotentials were calculated by correcting the standard thermodynamic potential, $E^0_{H^+/H_2}$ at the given pK_a of the acid used in the MeCN electrolyte.

Conclusions

Herein we report the synthesis of two novel Ni^{II} complexes supported by the N2S2 or NCHS2 ligands. The design of both Ni complexes was inspired by the biological HER catalysts [NiFe] hydrogenases. Remarkably, both $\mathbf{1}^{2+}$ and **2** achieved stable catalytic current with high turnover for proton reduction at a low concentration of added acid (0.043 M of TFA) in wet MeCN at the low cost of applied overpotential, ≤ 0.45 V. These results are significantly impressive as most of the Ni^{II}-based literature known HER electrocatalysts operate at a high acid concentration in the organic electrolyte. By comparison, under identical electrochemical conditions, $\mathbf{2}^{2+}$ showed comparatively faster reaction kinetics for HER than $\mathbf{1}^{2+}$, without compromising the overpotential. We attribute the improved HER catalytic properties of $\mathbf{2}^{2+}$ to the fast protonation of the protonated pyridyl group of the coordinating NCHS2 ligand upon activation of unligated C–H bond of the

chelating NCHS2 ligand, followed by the electrochemically reduction of Ni^{II} center to a catalytically active Ni^{I} species. We propose that such a protonation step is involved with the formation of Ni^{III}-hydride species and thus mimics the intermediates observed for [NiFe] hydrogenase during the biological HER process. Overall, we report two Ni^{II} molecular electrocatalysts, **1•(OTf)$_2$** and **2** that set a new electrocatalytic platform for proton reduction that show high turnover at the very low acid concentration in the organic electrolyte, without a high cost of overpotential.

METHODS

Reagents and Materials. All manipulations were carried out under a nitrogen atmosphere using standard Schlenk and glovebox techniques, if not indicated otherwise. All chemicals were commercially available from Aldrich, Fisher, or Strem Chemicals and were used as received without further purification. Solvents were purified prior to use by passing through a column of activated alumina using an MBraun solvent purification system.

Syntheses and characterization. Detail synthesis procedures and characterization data for our proposed ligands, N2S2 and NCHS2, and their corresponding Ni^{II} complexes are provided in the Supporting Information.

Electrochemistry. Electrochemical experiments were carried out using BASi Epsilon and CH Instruments potentiostats. Cyclic voltammetry used conventional three-electrode cell with a glassy carbon (GC) working electrode (surface area = 0.07 cm^2), a non-aqueous Ag/0.01 M $AgNO_3$/MeCN reference electrode, and a Pt wire counter electrode. The GC electrode was prepared by polishing on a cloth polishing pad using 5-micron aluminum oxide polishing slurry, followed by a thorough deionized water rinse, and gently drying with a heat gun.[57] Cyclic

voltammograms (CVs) were recorded by dissolving the metal complexes to 1.5 mM in 0.1 M of $^{n}Bu_4NPF_6$ ($TBAPF_6$) in MeCN, with or without the addition of protic additives, at 0.1 V/s scan rate unless otherwise noted. Ferrocene was used as an external standard for all the electrochemical experiments, and all potentials are reported with respect to the ferrocenium-ferrocene couple ($Fc^{+/0}$).[68] All CV data are plotted according to the US convention,[57] where the positive and negative currents are for the reduction and oxidation processes, respectively.

DATA AVAILABILITY

Supporting Information. Experimental details for the synthesis methodologies, spectroscopic characterization, supporting electrochemical data, and X-ray crystallographic data are available in the Supplementary Information. Crystallographic data for compounds NCHS2, **1•(OTf)$_2$**, **2**, and **5'** are available free of charge from the Cambridge Crystallographic Data Centre (CCDC) under reference numbers 2053834, 2053835, 2053836, and 2053837, respectively.

AUTHOR INFORMATION

Corresponding Author

*Department of Chemistry, University of Illinois-Urbana Champaign, 600 S. Mathews Avenue, Urbana, IL, 61801, USA.

Email: mirica@illinois.edu

ORCID

Liviu M. Mirica: 0000-0003-0584-9508

Soumalya Sinha: 0000-0002-6212-1102

ACKNOWLEDGMENTS

We thank the Department of Energy's BES Catalysis Science Program (DE-SC0006862) for financial support of the initial studies. We thank all the research facilities in the Department of Chemistry at the University of Illinois at Urbana-Champaign for their help. We also thank Leonel Griego for discussions related to EPR data analysis.

AUTHOR CONTRIBUTIONS

L.M.M. directed the overall research project. S.S. and G.N.T performed the experiments and analysed the experimental data. H.N. obtained and analyzed the data for the crystal structure of **5'**. N.P.R. analyzed the crystal structure data for NCHS2, **1•(OTf)$_2$**, and **2**. All authors contributed to the preparation of the manuscript. S.S. and G.N.T. contributed equally to this work.

REFERENCES

1. Lewis, N. S.; Nocera, D. G. Powering the planet: Chemical challenges in solar energy utilization *Proc. Nat. Acad. Sci. USA* **2006**, *103*, 15729.
2. Nocera, D. G. The Artificial Leaf *Acc. Chem. Res.* **2012**, *45*, 767.
3. Laursen, A. B.; Kegnæs, S.; Dahl, S.; Chorkendorff, I. Molybdenum sulfides—efficient and viable materials for electro - and photoelectrocatalytic hydrogen evolution *Energy Environ. Sci.* **2012**, *5*, 5577.
4. Wang, M.; Chen, L.; Sun, L. Recent progress in electrochemical hydrogen production with earth-abundant metal complexes as catalysts *Energy Environ. Sci.* **2012**, *5*, 6763.
5. Popczun, E. J.; McKone, J. R.; Read, C. G.; Biacchi, A. J.; Wiltrout, A. M.; Lewis, N. S.; Schaak, R. E. Nanostructured Nickel Phosphide as an Electrocatalyst for the Hydrogen Evolution Reaction *J. Am. Chem. Soc.* **2013**, *135*, 9267.
6. Jones, A. K.; Sillery, E.; Albracht, S. P.; Armstrong, F. A. Direct comparison of the electrocatalytic oxidation of hydrogen by an enzyme and a platinum catalyst *Chem Commun (Camb)* **2002**, 866.
7. Cammack, R. Hydrogenase sophistication *Nature* **1999**, *397*, 214.
8. Madden, C.; Vaughn, M. D.; Diez-Perez, I.; Brown, K. A.; King, P. W.; Gust, D.; Moore, A. L.; Moore, T. A. Catalytic turnover of [FeFe]-hydrogenase based on single-molecule imaging *J. Am. Chem. Soc.* **2012**, *134*, 1577.
9. Gan, L.; Groy, T. L.; Tarakeshwar, P.; Mazinani, S. K.; Shearer, J.; Mujica, V.; Jones, A. K. A nickel phosphine complex as a fast and efficient hydrogen production catalyst *J. Am. Chem. Soc.* **2015**, *137*, 1109.

10. Das, R.; Neese, F.; van Gastel, M. Hydrogen evolution in [NiFe] hydrogenases and related biomimetic systems: similarities and differences *Phys. Chem. Chem. Phys.* **2016**, *18*, 24681.
11. De Lacey, A. L.; Fernandez, V. M.; Rousset, M.; Cammack, R. Activation and inactivation of hydrogenase function and the catalytic cycle: spectroelectrochemical studies *Chem. Rev.* **2007**, *107*, 4304.
12. Siegbahn, P. E.; Tye, J. W.; Hall, M. B. Computational studies of [NiFe] and [FeFe] hydrogenases *Chem. Rev.* **2007**, *107*, 4414.
13. Lubitz, W.; Ogata, H.; Rudiger, O.; Reijerse, E. Hydrogenases *Chem. Rev.* **2014**, *114*, 4081.
14. Artz, J. H.; Zadvornyy, O. A.; Mulder, D. W.; King, P. W.; Peters, J. W. In *Methods in Enzymology*; David, S. S., Ed.; Academic Press, 2017; Vol. 595, p. 213.
15. Whitehead, J. P.; Gurbiel, R. J.; Bagyinka, C.; Hoffman, B. M.; Maroney, M. J. The hydrogen binding site in hydrogenase: 35-GHz ENDOR and XAS studies of the nickel-C (reduced and active form) and the Ni-L photoproduct *J. Am. Chem. Soc.* **1993**, *115*, 5629.
16. Schilter, D.; Camara, J. M.; Huynh, M. T.; Hammes-Schiffer, S.; Rauchfuss, T. B. Hydrogenase Enzymes and Their Synthetic Models: The Role of Metal Hydrides *Chem. Rev.* **2016**, *116*, 8693.
17. Murphy, B. J.; Hidalgo, R.; Roessler, M. M.; Evans, R. M.; Ash, P. A.; Myers, W. K.; Vincent, K. A.; Armstrong, F. A. Discovery of Dark pH-Dependent H+ Migration in a [NiFe]-Hydrogenase and Its Mechanistic Relevance: Mobilizing the Hydrido Ligand of the Ni-C Intermediate *J. Am. Chem. Soc.* **2015**, *137*, 8484.
18. Greene, B. L.; Wu, C.-H.; McTernan, P. M.; Adams, M. W. W.; Dyer, R. B. Proton-Coupled Electron Transfer Dynamics in the Catalytic Mechanism of a [NiFe]-Hydrogenase *J. Am. Chem. Soc.* **2015**, *137*, 4558.
19. Hidalgo, R.; Ash, P. A.; Healy, A. J.; Vincent, K. A. Infrared Spectroscopy During Electrocatalytic Turnover Reveals the Ni-L Active Site State During H2 Oxidation by a NiFe Hydrogenase *Angew. Chem., Int. Ed.* **2015**, *54*, 7110.
20. Barton, B. E.; Whaley, C. M.; Rauchfuss, T. B.; Gray, D. L. Nickel-iron dithiolato hydrides relevant to the [NiFe]-hydrogenase active site *J. Am. Chem. Soc.* **2009**, *131*, 6942.
21. Barton, B. E.; Rauchfuss, T. B. Hydride-containing models for the active site of the nickel-iron hydrogenases *J. Am. Chem. Soc.* **2010**, *132*, 14877.
22. Schilter, D.; Nilges, M. J.; Chakrabarti, M.; Lindahl, P. A.; Rauchfuss, T. B.; Stein, M. Mixed-valence nickel-iron dithiolate models of the [NiFe]-hydrogenase active site *Inorg. Chem.* **2012**, *51*, 2338.
23. Tard, C.; Pickett, C. J. Structural and functional analogues of the active sites of the [Fe]-, [NiFe]-, and [FeFe]-hydrogenases *Chem. Rev.* **2009**, *109*, 2245.
24. Evans, D. J.; Pickett, C. J. Chemistry and the hydrogenases *Chem. Soc. Rev.* **2003**, *32*, 268.
25. Basu, D.; Bailey, T. S.; Lalaoui, N.; Richers, C. P.; Woods, T. J.; Rauchfuss, T. B.; Arrigoni, F.; Zampella, G. Synthetic Designs and Structural Investigations of Biomimetic Ni-Fe Thiolates *Inorg. Chem.* **2019**, *58*, 2430.

26. Efros, L. L.; Thorp, H. H.; Brudvig, G. W.; Crabtree, R. H. Toward a Functional Model of Hydrogenase: Electrocatalytic Reduction of Protons to Dihydrogen by a Nickel Macrocyclic Complex *Inorg. Chem.* **1992**, *31*, 1722.
27. Lai, K.-T.; Ho, W.-C.; Chiou, T.-W.; Liaw, W.-F. Formation of [NiIII(κ1-S2CH)(P(o-C6H3-3-SiMe3-2-S)3)]− via CS2 Insertion into Nickel(III) Hydride Containing [NiIII(H)(P(o-C6H3-3-SiMe3-2-S)3)]− *Inorg. Chem.* **2013**, *52*, 4151.
28. Gu, N. X.; Oyala, P. H.; Peters, J. C. H2 Evolution from a Thiolate-Bound Ni(III) Hydride *J. Am. Chem. Soc.* **2020**, *142*, 7827.
29. Wilson, A. D.; Newell, R. H.; McNevin, M. J.; Muckerman, J. T.; Rakowski DuBois, M.; DuBois, D. L. Hydrogen Oxidation and Production Using Nickel-Based Molecular Catalysts with Positioned Proton Relays *J. Am. Chem. Soc.* **2006**, *128*, 358.
30. Wilson, A. D.; Shoemaker, R. K.; Miedaner, A.; Muckerman, J. T.; DuBois, D. L.; DuBois, M. R. Nature of hydrogen interactions with Ni(II) complexes containing cyclic phosphine ligands with pendant nitrogen bases *Proc. Natl. Acad. Sci. U. S. A.* **2007**, *104*, 6951.
31. Kilgore, U. J.; Roberts, J. A. S.; Pool, D. H.; Appel, A. M.; Stewart, M. P.; DuBois, M. R.; Dougherty, W. G.; Kassel, W. S.; Bullock, R. M.; DuBois, D. L. [Ni(PPh2NC6H4X2)2]2+ Complexes as Electrocatalysts for H2 Production: Effect of Substituents, Acids, and Water on Catalytic Rates *J. Am. Chem. Soc.* **2011**, *133*, 5861.
32. Helm, M. L.; Stewart, M. P.; Bullock, R. M.; DuBois, M. R.; DuBois, D. L. A Synthetic Nickel Electrocatalyst with a Turnover Frequency Above 100,000 s(-1) for H-2 Production *Science* **2011**, *333*, 863.
33. Hu, X.; Brunschwig, B. S.; Peters, J. C. Electrocatalytic hydrogen evolution at low overpotentials by cobalt macrocyclic glyoxime and tetraimine complexes *J. Am. Chem. Soc.* **2007**, *129*, 8988.
34. Jacques, P.-A.; Artero, V.; Pécaut, J.; Fontecave, M. Cobalt and nickel diimine-dioxime complexes as molecular electrocatalysts for hydrogen evolution with low overvoltages *Proc. Natl. Acad. Sci. U. S. A.* **2009**, *106*, 20627.
35. Dempsey, J. L.; Brunschwig, B. S.; Winkler, J. R.; Gray, H. B. Hydrogen Evolution Catalyzed by Cobaloximes *Acc. Chem. Res.* **2009**, *42*, 1995.
36. Liu, T.; Darensbourg, M. Y. A Mixed-Valent, Fe(II)Fe(I), Diiron Complex Reproduces the Unique Rotated State of the [FeFe]Hydrogenase Active Site *J. Am. Chem. Soc.* **2007**, *129*, 7008.
37. Kaur-Ghumaan, S.; Schwartz, L.; Lomoth, R.; Stein, M.; Ott, S. Catalytic Hydrogen Evolution from Mononuclear Iron(II) Carbonyl Complexes as Minimal Functional Models of the [FeFe] Hydrogenase Active Site *Angew. Chem., Int. Ed.* **2010**, *49*, 8033.
38. Gloaguen, F.; Rauchfuss, T. B. Small molecule mimics of hydrogenases: hydrides and redox *Chem. Soc. Rev.* **2009**, *38*, 100.
39. Fontecilla-Camps, J. C.; Volbeda, A.; Cavazza, C.; Nicolet, Y. Structure/Function Relationships of [NiFe]- and [FeFe]-Hydrogenases *Chem. Rev.* **2007**, *107*, 4273.

40. Vignais, P. M.; Billoud, B. Occurrence, Classification, and Biological Function of Hydrogenases: An Overview *Chem. Rev.* **2007**, *107*, 4206.
41. Ott, S.; Kritikos, M.; Akermark, B.; Sun, L.; Lomoth, R. A biomimetic pathway for hydrogen evolution from a model of the iron hydrogenase active site *Angew Chem Int Ed Engl* **2004**, *43*, 1006.
42. Schwartz, L.; Eilers, G.; Eriksson, L.; Gogoll, A.; Lomoth, R.; Ott, S. Iron hydrogenase active site mimic holding a proton and a hydride *Chem. Comm.* **2006**, 520.
43. Lawrence, J. D.; Li, H.; Rauchfuss, T. B.; Bénard, M.; Rohmer, M.-M. Diiron Azadithiolates as Models for the Iron-Only Hydrogenase Active Site: Synthesis, Structure, and Stereoelectronics *Angew. Chem., Int. Ed.* **2001**, *40*, 1768.
44. Barton, B. E.; Olsen, M. T.; Rauchfuss, T. B. Aza- and oxadithiolates are probable proton relays in functional models for the [FeFe]-hydrogenases *J. Am. Chem. Soc.* **2008**, *130*, 16834.
45. Wiese, S.; Kilgore, U. J.; Ho, M.-H.; Raugei, S.; DuBois, D. L.; Bullock, R. M.; Helm, M. L. Hydrogen Production Using Nickel Electrocatalysts with Pendant Amines: Ligand Effects on Rates and Overpotentials *ACS Catal.* **2013**, *3*, 2527.
46. McCarthy, B. D.; Martin, D. J.; Rountree, E. S.; Ullman, A. C.; Dempsey, J. L. Electrochemical Reduction of Brønsted Acids by Glassy Carbon in Acetonitrile—Implications for Electrocatalytic Hydrogen Evolution *Inorg. Chem.* **2014**, *53*, 8350.
47. Rountree, E. S.; Dempsey, J. L. Potential-Dependent Electrocatalytic Pathways: Controlling Reactivity with pK(a) for Mechanistic Investigation of a Nickel-Based Hydrogen Evolution Catalyst *J. Am. Chem. Soc.* **2015**, *137*, 13371.
48. Tatematsu, R.; Inomata, T.; Ozawa, T.; Masuda, H. Electrocatalytic Hydrogen Production by a Nickel(II) Complex with a Phosphinopyridyl Ligand *Angew. Chem., Int. Ed.* **2016**, *55*, 5247.
49. Barrón, D.; Butí, S.; Ruiz, M.; Barbosa, J. Evaluation of acidity constants and preferential solvation in tetrahydrofuran–water mixtures *Polyhedron* **1999**, *18*, 3281.
50. DuBois, D. L.; Bullock, R. M. Molecular Electrocatalysts for the Oxidation of Hydrogen and the Production of Hydrogen – The Role of Pendant Amines as Proton Relays *Eur. J. Inorg. Chem.* **2011**, *2011*, 1017.
51. Passard, G.; Dogutan, D. K.; Qiu, M.; Costentin, C.; Nocera, D. G. Oxygen Reduction Reaction Promoted by Manganese Porphyrins *ACS Catal.* **2018**, *8*, 8671.
52. Moriguchi, T.; Kitamura, S.; Sakata, K.; Tsuge, A. Syntheses and Structures of Dichloropalladium(II)(Dithia[3.3]Metadipyridinophane) and Dichloroplatinum(II)(Dithia[3.3]Metadipyridinophane) Complexes *Polyhedron* **2001**, *20*, 2315.
53. See Supporting Information.
54. Addison, A. W.; Rao, T. N.; Reedijk, J.; van Rijn, J.; Verschoor, G. C. Synthesis, structure, and spectroscopic properties of copper(II) compounds containing nitrogen sulfur donor ligands - the crystal and molecular structure of aqua[1,7-bis(N-methylbenzimidazol-2'-yl)-2,6-dithiaheptane]copper(II) perchlorate *J. Chem. Soc., Dalton Trans.* **1984**, 1349.

55. Zhou, W.; Zheng, S. A.; Schultz, J. W.; Rath, N. P.; Mirica, L. M. Aromatic Cyanoalkylation through Double C-H Activation Mediated by Ni(III) *J. Am. Chem. Soc.* **2016**, *138*, 5777.
56. Bard, A. J. Fundamentals and applications **2001**, *2*, 580.
57. Elgrishi, N.; Rountree, K. J.; McCarthy, B. D.; Rountree, E. S.; Eisenhart, T. T.; Dempsey, J. L. A Practical Beginner's Guide to Cyclic Voltammetry *J. Chem. Educ.* **2018**, *95*, 197.
58. Savéant, J.-M.; Costentin, C. *Elements of Molecular and Biomolecular Electrochemistry: An Electrochemical Approach to Electron Transfer Chemistry*; 2nd ed., 2019.
59. Richburg, C. S.; Farnum, B. H. Influence of Pyridine on the Multielectron Redox Cycle of Nickel Diethyldithiocarbamate *Inorg. Chem.* **2019**, *58*, 15371.
60. Lapointe, D.; Fagnou, K. Overview of the Mechanistic Work on the Concerted Metallation–Deprotonation Pathway *Chem. Lett.* **2010**, *39*, 1118.
61. Zhou, W.; Rath, N. P.; Mirica, L. M. Oxidatively-induced aromatic cyanation mediated by Ni(III) *Dalton Trans.* **2016**, *45*, 8693.
62. Sinha, S.; Warren, J. J. Unexpected Solvent Effect in Electrocatalytic CO2 to CO Conversion Revealed Using Asymmetric Metalloporphyrins *Inorg. Chem.* **2018**, *57*, 12650.
63. Costentin, C.; Passard, G.; Robert, M.; Savéant, J.-M. Pendant Acid–Base Groups in Molecular Catalysts: H-Bond Promoters or Proton Relays? Mechanisms of the Conversion of CO2 to CO by Electrogenerated Iron(0)Porphyrins Bearing Prepositioned Phenol Functionalities *J. Am. Chem. Soc.* **2014**, *136*, 11821.
64. Martin, D. J.; McCarthy, B. D.; Donley, C. L.; Dempsey, J. L. Electrochemical hydrogenation of a homogeneous nickel complex to form a surface adsorbed hydrogen-evolving species *Chem. Comm.* **2015**, *51*, 5290.
65. Costentin, C.; Savéant, J.-M. Multielectron, Multistep Molecular Catalysis of Electrochemical Reactions: Benchmarking of Homogeneous Catalysts *ChemElectroChem* **2014**, *1*, 1226.
66. Artero, V.; Saveant, J.-M. Toward the rational benchmarking of homogeneous H2-evolving catalysts *Energy Environ. Sci.* **2014**, *7*, 3808.
67. Appel, A. M.; Helm, M. L. Determining the Overpotential for a Molecular Electrocatalyst *ACS Catal.* **2014**, *4*, 630.
68. Pavlishchuk, V. V.; Addison, A. W. Conversion constants for redox potentials measured versus different reference electrodes in acetonitrile solutions at 25°C *Inorg. Chim. Acta* **2000**, *298*, 97.

Table of Contents Graphic

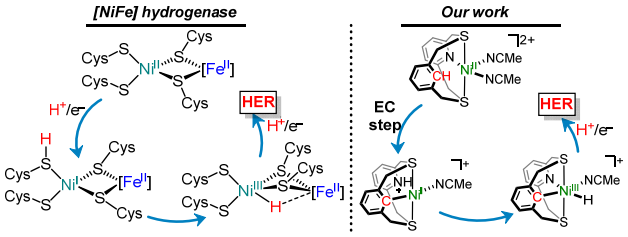

Synopsis

Electrocatalytic hydrogen evolution at a low overpotential and with high turnover frequency in the presence of low acid concentration was observed for a novel bioinspired (NCS2)Ni(II) complex that is proposed to involve an organometallic intermediate.